Probing the structure, the composition and the ORR activity of Pt₃Co/C nanocrystallites during a 3422 h PEMFC ageing test

Laetitia Dubau [a,*], Miguel Lopez-Haro [a,b], Luis Castanheira [a], Julien Durst [a], Marian Chatenet [a], Pascale Bayle-Guillemaud [b], Laure Guétaz [c], Nicolas Caqué [d], Elisabeth Rossinot [d], Frédéric Maillard [a,*]

[a] Laboratoire d'Electrochimie et de Physico-chimie des Matériaux et des Interfaces, UMR 5279 CNRS/Grenoble-INP/Université de Savoie/Université Joseph Fourier, 1130 rue de la piscine, BP75, 38402 Saint Martin d'Hères Cedex, France
[b] CEA-INAC/UJF-Grenoble 1 UMR-E, SP2M, LEMMA, Minatec, 38054 Grenoble Cedex 9, France
[c] CEA-LITEN, Département des Technologies de l'Hydrogène, Laboratoire des Composants PEM, 17 rue des Martyrs, 38054 Grenoble, France
[d] Axane, 2 rue de Clémencière, BP 15, 38360 Sassenage, France

ARTICLE INFO

ABSTRACT

Long-term (3422 h) operation of proton exchange membrane fuel cell in stationary conditions causes two regimes of degradation of the cathode catalytic layer. Firstly, from the beginning of life until the first membrane electrode assembly sampling, at t = 1163 h, fast degradation of the fresh Pt₃Co/C nanoparticles is monitored; classical degradation mechanisms of Pt-based electrocatalysts occur, such as carbon corrosion, crystallite migration, dissolution of the less noble metal (Co), and 3D Ostwald ripening. A second degradation regime sets up from 1163 h to 3422 h, during which the changes in composition and morphology are slower. At the end of the ageing test, three distinct populations of Pt–Co/C nanoparticles coexist: (i) Pt–Co/C core–shell particles characterized by an alloyed (but depleted, compared to the fresh material) core surrounded by a 3–5 monolayer thick Pt-rich shell, (ii) Pt–Co/C "hollow" particles containing a central cavity surrounded by a Pt–Co shell containing limited amount of Co atoms distributed at the atomic scale and (iii) pure Pt/C "hollow" particles, from which Co dissolution has been completed. Experimental evidences are provided that the Pt-rich phase remains stable, and maintains constant ORR activity over more than 2000 h of operation in real PEMFC conditions.

© 2013 Elsevier B.V. All rights reserved.

1. Introduction

The ever-growing energy demand worldwide and the announced end of the so-called "fossil fuel era" are currently boosting the development of electrochemical energy technologies, such as fuel cells, batteries and supercapacitors. The present paper concerns the former systems, with special emphasis on low-temperature proton-exchange membrane fuel cells (PEMFCs). PEMFCs ionize hydrogen into protons and electrons at the anode, both species flowing to the cathode to participate in the oxygen reduction reaction (ORR). Although PEMFCs are the more advanced high-energy-density electrochemical generators, their massive production still requires to overcome several hurdles: (i) improving the ORR activity, (ii) decreasing the cost of the catalytic layers (low amount of noble metal) and (iii) improving the durability of the cathodic material [1].

To that goals, extended surface area or nanometre sized Pt–M bimetallic alloys, where M is a less expensive transition metal such as Co, [2–8] Fe, [3,5–7,9] Cu, [10] or Ni [4,6,7,11–14], are now widely used as cathodic electrocatalysts. They feature 2–5 times ORR activity gain over pure Pt/C crystallites of the same size, and this gain can be finely tailored by controlling the atomic arrangement in the few topmost layers (the so-called "Pt-skin" or "Pt-skeleton" approach), [13,15–18] by electrochemical/chemical dealloying [10,19] or by controlling the orientation of the facets [14,20–23]. Decreasing the cost of the catalytic layer (CL) can also be achieved by using nanoparticles composed of one or several Pt monolayer(s) deposited on a less noble and less costly metal core (e.g. Pt/Co, Pt/Ni), that is itself covered by Pd (e.g. Pt/Pd/Co) [24,25]. Ultimately, the prohibitive cost of Pt can be suppressed by using non-precious metal catalysts, but these materials still suffer from high mass-transport losses and/or lack of stability on the long-term [26–29].

To date, alloyed bimetallic catalysts represent the more widespread strategy to deploy the PEMFC technology at a large scale, but their long-term stability remains controversial. Whereas some authors claim that bimetallic alloys maintain their better

* Corresponding author.
E-mail addresses: laetitia.dubau@lepmi.grenoble-inp.fr (L. Dubau),
frederic.maillard@lepmi.grenoble-inp.fr (F. Maillard).

catalytic performance over time, [3,6,11,30] recent experimental [8,31–36] and theoretical [37–40] studies performed on Pt–Co/C have assessed that the bimetallic nanocrystallites are continuously depleted in Co, yielding decreased ORR activity. The loss in ORR catalytic activity not only arises from the fact that Co is leached out from the fresh catalyst but also because Co^{2+} ions favour surface oxide formation at the catalytic surface, and negatively affect the O_2 mass-transport properties to the catalytic surface [41]. Long-term changes in the morphology of the fresh alloy essentially depend on the initial non-noble metal content, [42,43] the crystallite size, [43] the gas atmosphere, [44] and the electrochemical potential range experienced during fuel cell operation [36,45]. Various structures have been found in aged catalytic layers composed of alloyed nanocrystallites with a size below 6–8 nm: homogeneously alloyed, [35] core–shell, [17,35,36,43,46] "spongy" or "swiss cheese" [16,17,33,46,47] and "hollow" [36] nanocrystallites. Larger or Co-richer particles yield different structures: particles with an initial size of *ca.* 10–30 nm form multiple core–shell structures, and a transition towards nanoporous materials is observed for particles larger than 30 nm [43]. Extended surface area catalysts, such as nanostructured-thin-films or Pt-alloy wires and nanotubes, are no exception and loss of the less noble metal has already been reported by membrane electrode assembly (MEA) manufacturers [48–50].

The corrosion of the high surface area carbon support is thermodynamically possible for $E > 0.207$ V *vs.* the normal hydrogen electrode under standard conditions; therefore it is mainly occurring at the cathode. The carbon oxidation reaction (COR) yields detachment of the Pt-based nanoparticles, and ultimately results in amorphization, and therefore loss of electrical conductivity, of the carbon support. Oxygen-containing carbon surface groups formed by the COR at $E > 0.3$ V *vs.* RHE (where RHE stands for Reversible Hydrogen Electrode) have been detected with electrochemical-infrared spectroscopy, these groups being converted into CO_2 at $E > 0.60$ V *vs.* RHE, as measured by differential electrochemical mass spectroscopy [51,52], this reaction being catalysed by the metal nanoparticles [51–55]. The extent of graphitization of the carbon support plays an important role on its stability, graphitic carbons being more thermally and electrochemically stable [54,56–58]. Dynamic PEMFC conditions such as start-up/shut down accelerate the rate of the COR with respect to normal fuel cell operation, [59–61] and recent studies using segmented cells have shown that the cathode region facing the H_2 outlet suffers severe corrosion [60,62]. Since corrosion of the metal phase and the carbon support are strongly inter-related, they must be studied simultaneously in real PEMFC conditions. Detailed investigations of the changes of both the metal phase and the carbon support over time are also keys to propose new strategies towards the mitigation of the PEMFC materials degradation.

In this study, conventional and advanced transmission electron microscopy and X-ray based techniques are used to provide new insights on the long-term modification of Pt_3Co/C nanocrystallites ($t = 3422$ h) in real PEMFC conditions (16-cell stack, H_2/air, $I = 50$ A, $T = 70$ °C, 65% relative humidity at the cathode, dead-end mode at the anode). Efforts are paid to cover both the carbon support and the metal phase at various length scales, from the micrometre to the atom.

2. Experimental

2.1. PEMFC testing

A 16-cell short PEMFC stack based on Pt/C at the anode and Pt_3Co/C at the cathode was operated at constant current ($I = 50$ A, translating into an average current density of $j = 0.60$ A cm^{-2}) for $t = 3422$ h. The cathode was fed with humidified air (65% relative humidity (RH), 1.1 bar abs., gas stoichiometry of 2.5), and the relative humidity was fixed at the gas inlet by an adequate choice of the humidifier and cell temperatures. The anode was fuelled with dry pure dihydrogen (0% RH, 1.3 bar abs., dead-end mode, corresponding to an average H_2 stoichiometry of *ca.* 1). The gas flow rates were 5.6 and 33.2 N L min^{-1} for H_2 and air, respectively. Air and H_2 purges were performed intermittently to remove the water produced at the cathode and the water/nitrogen that accumulate at the anode, respectively.

The stacks were disassembled after different life stages for real-time characterizations: some of the membrane electrode assemblies (MEAs) were removed and used for physical, chemical and electrochemical measurements in liquid electrolyte (cell 10 after 1163 and 2259 h of operation and cell 8 after 3422 h of operation. Those cells were located in the middle of the stack, thus ensuring reproducible and well-controlled ageing conditions). After their replacement by fresh MEAs, the stack was re-conditioned and then re-operated (see [34,35] for more details). All the data presented in the following sections were obtained for electrocatalysts sampled in the cathode inlet region of the MEA, which is the region of harshest degradation in the present operating conditions [63].

2.2. Field emission gun – scanning electron microscopy (FEG-SEM) imaging

FEG-SEM images were obtained on a Zeiss Ultra 55 microscope designed to maximize the image resolution at low beam energies. The Ultra 55 is equipped with a secondary electron detector inside the lens (in lens detector) and a backscattered electron detector. Both are engineered to image electrons at low accelerating voltage (less than 5 kV). The samples consisted of circular or square zones cut fresh/aged CLs (gas inlet region). The measurement of the component thickness was done by integrating the overall thickness of the electrodes or membrane with ImageJ® freeware.

2.3. Transmission electron microscopy (TEM), high angle annular dark field (HAADF) and electron energy loss spectroscopy (EELS)

In transmission electron microscopy (TEM) measurements, Pt–Co/C powder scraped from the fresh/aged CLs was deposited on a copper grid bearing a Lacey carbon membrane. The samples were observed with a Jeol 2010 TEM operated at 200 kV with a point to point resolution of 0.19 nm (LaB$_6$ filament) and the particle size distribution of fresh and aged catalysts were determined by counting at least 400 individual (and round-shaped) particles from representative images.

For each distribution, the number-averaged diameter: $\bar{d}_N = \sum_{i=1}^{m} n_i d_i / \sum_{i=1}^{m} n_i$, and the surface-averaged diameter: $\bar{d}_S = \sum_{i=1}^{m} n_i d_i^3 / \sum_{i=1}^{m} n_i d_i^2$ were determined (where n_i stands for the number of particles having a diameter d_i). We also used TEM images to evaluate the number of isolated/aggregated particles per geometrical μm^2 of carbon by eye-counting over typically 20 representative TEM images (TEM images are two-dimension projections of three-dimension Pt–Co/C electrocatalysts).

To investigate the chemical distribution of Pt and Co on the fresh/aged Pt–Co/C cathode electrocatalysts, we combined the capabilities of the aberration-corrected scanning transmission electron microscope with electron energy loss spectroscopy (EELS), working in spectrum image (SI) mode. In this mode, one EELS spectrum and the high angle annular dark field (HAADF) signal were both collected at each point in the scan. This allowed correlating the nanoanalytical and nanostructural information in the Pt-based alloy nanocatalysts. The SI analysis was performed on a FEI-Titan Ultimate microscope operated at 200 kV and corrected to fourth-order aberrations, using 20 mrad and 73 mrad convergence

and collection semi-angles, respectively. To compensate for possible sample drift during the analysis, a spatial drift correction was used on every line of the analysis. Every spectrum was acquired using an acquisition time of 100 ms and an energy dispersion of 0.3 eV per channel. The matrix of spectra was de-noised using the standard principal component analysis and chemical maps were constructed analysing the Pt N_3 (518 eV) and Co $L_{2,3}$ (780 eV) edges using a power-law background subtraction [64,65].

2.4. X-ray diffraction (XRD) measurements

A cylinder of *ca.* 1 cm^2 was cut in the inlet region of the cathode CL with a punch and analysed using a Philips TW 1730 vertical goniometer/diffractometer equipped with a diffracted-beam monochromator using Cu($K_{\alpha 1}$) radiation (λ = 0.15406 nm).

2.5. Raman spectroscopy

Raman spectroscopy was used to examine the extent of graphitization of the fresh/aged carbon supports. The Raman spectra were recorded *ex situ* using either a Renishaw RM1000 or a Renishaw In-Via spectrometer. The Raman spectra were obtained by using an argon LASER (514 nm) operated at approximately 5 mW. The detector was a Peltier-cooled charge coupled device camera (CCD) and the spectral resolution was about 1 cm^{-1}. The measurements were performed with a ×50 ULWD objective and a 100 μm confocal aperture for both the sample illumination and collection of the scattered photons.

2.6. Electrochemical measurements in liquid electrolyte

2.6.1. Solutions

All the glassware used in this work was cleaned by immersion in a H_2SO_4:H_2O_2 mixture overnight and thoroughly rinsed with Milli-Q water (18.2 MΩ cm, 1–3 ppm TOC). The electrolytic solutions were prepared from Milli-Q water and H_2SO_4 (Suprapur, Merck).

2.6.2. Preparation of the thin-film RDE and electrochemical measurements

All the details about the electrochemical set-up, the preparation of rotating disc electrodes (RDE) can be found in Ref. [36]. Only one exception concerned the determination of the ORR activity of the fresh/aged Pt–Co/C and Pt/C electrodes. Linear sweep experiments were conducted in O_2-saturated 0.1 M H_2SO_4 solution by sweeping the potential from 0.40 to 1.05 V at a scan rate of 2 mV s^{-1} and a revolution rate of 1600 rpm. The ORR specific activity was determined at E = 0.85 or 0.90 V *vs.* RHE by normalizing the current measured after correction from the oxygen diffusion in the solution to the real surface area determined by CO stripping voltammetry.

3. Results and discussion

3.1. Morphological changes

3.1.1. At the micrometre scale: thickness of the cathode

Fig. 1 shows representative FEG-SEM images of the MEAs in their initial state and after ageing for t = 1163 h, 2259 h or 3422 h. The cathode, the brighter electrode in back-scattered electrons (BSE) mode due to the higher metal loading and corresponding larger average atomic number, suffers drastic changes over time. Firstly, its continuous thinning is observed, yielding detachment from the PEM in some places or ultimately its complete depletion. On the contrary, the anode remains essentially unaffected, except at t = 3422 h for which it is no longer attached to the PEM (but this likely originates from the severe MEA degradation at that stage and not to anode degradations). The cathode thickness decreased in average from 13.5 μm for the fresh MEA to 5 μm after 1163 h and
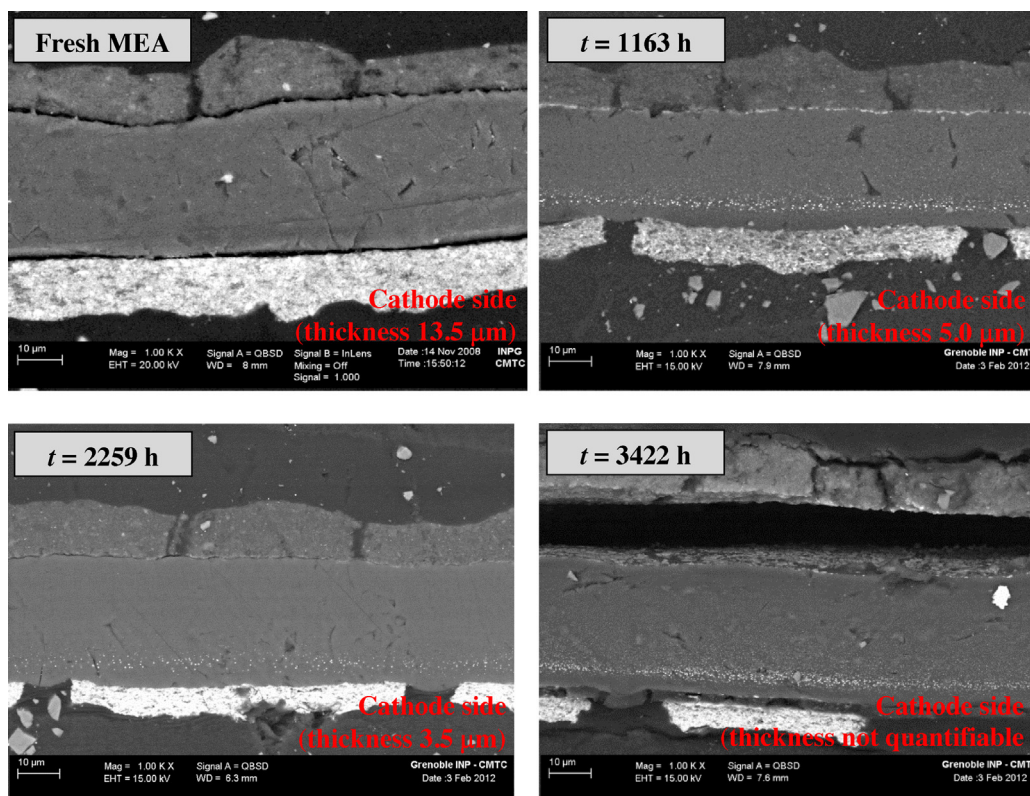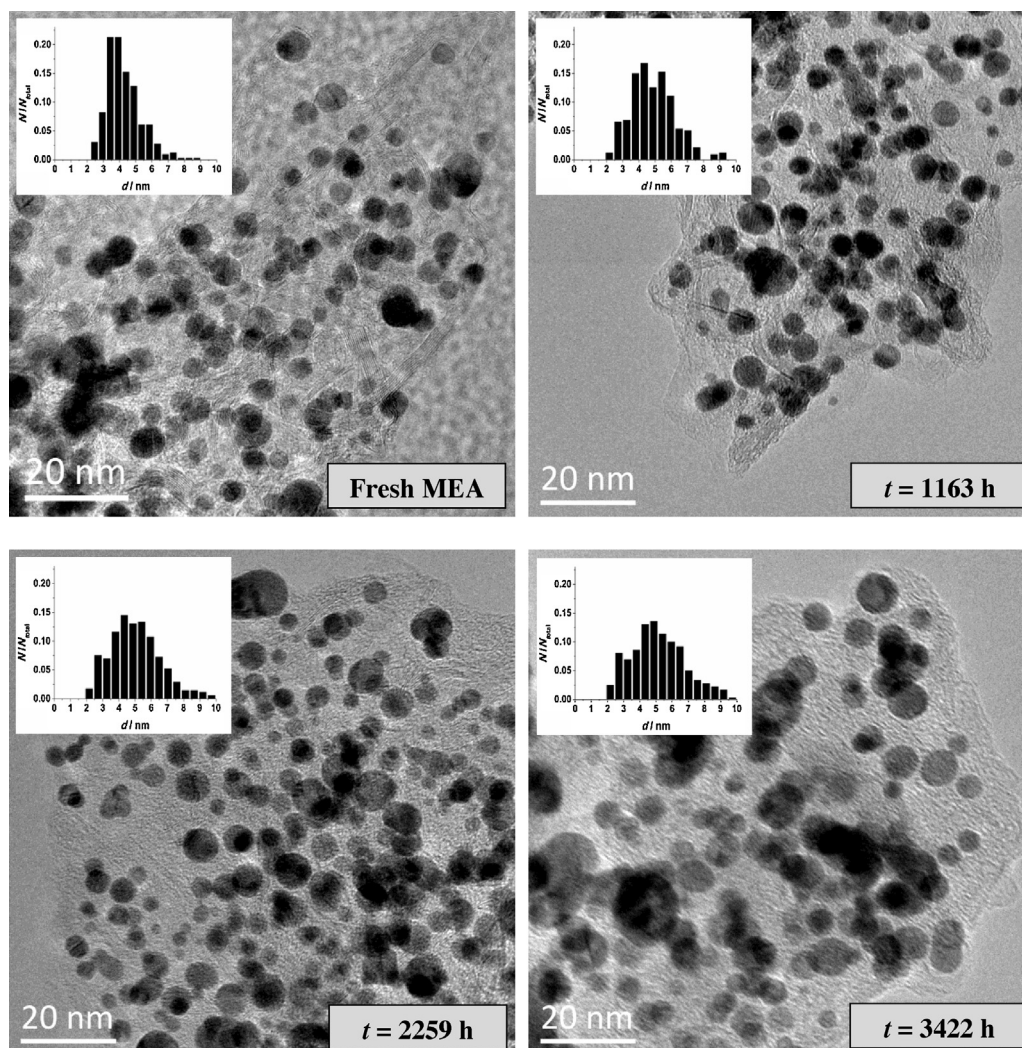

Fig. 1. FEG-SEM images obtained in back-scattered electrons for MEAs operated at I = 50 A–T = 70 °C–65% RH after various durations of operation.

Fig. 2. Particle size distributions and representative TEM images of the Pt–Co/C cathode electrocatalyst before/after operation at $I = 50$ A–$T = 70\,°C$–65% RH for various durations.

to 3.5 μm after 2259 h of operation. It could not be estimated properly after 3422 h of ageing, since the electrode was too damaged at that stage (absence or severe cracking of the cathodic CL in some regions). The latter undeniably signs carbon corrosion; this issue will be discussed later (see Section 3.1.3).

As observed previously with Pt/C [66,67] and Pt$_3$Co/C-based cathodes, [33,34] a "Pt band" is observed in the PEM *ca.* 4 μm away from the interface with the cathode after 1163 h of ageing. This band becomes coarser and brighter (the imaged were collected in BSE mode) upon ageing, assessing the corrosion of the cathode bimetallic alloy followed by the re-deposition of Pt^{z+} species in the PEM upon chemical reduction by H$_2$ crossing-over from the anode [68,69]. As shown in previous studies, Co cannot be thermodynamically reduced by H$_2$ [33,34], and Pt–Co particles in the PEM are unlikely to form because of the low enthalpy of mixing of Pt–Co alloys (*ca.* −10 kJ mol^{-1}, see [33]), which explains why Co species were not detected in the PEM by energy dispersive X-ray spectroscopy (X-EDS) analyses [32,34].

### 3.1.2. At the nanometre scale: crystallite migration and 3D Ostwald ripening

Fig. 2 presents particle size distributions and representative TEM images of the Pt–Co/C cathode catalyst during PEMFC operation. During the PEMFC ageing test, the centre of the Pt–Co/C particle size histogram shifts towards larger particle sizes by *ca.* 1.5 nm, and

a long tailing towards larger particle sizes concomitantly develops. A clear increase of the fraction of aggregated Pt–Co/C nanoparticles is also witnessed, the aged Pt–Co/C nanoparticles featuring complex shapes, suggesting particle overlap, coalescence and/or particle necking by Pt^{z+} ions redepositing between two individual crystallites.

This result is statistically confirmed in Fig. 3, in which the density of isolated and aggregated particles estimated from TEM images is plotted as a function of the PEMFC operation time. Interestingly, two distinct regimes are monitored: during the first 1163 h of operation, a severe decrease of the density of isolated Pt–Co/C particles is observed (two third of the isolated Pt–Co/C particles are lost during this time period), whereas for the following 2200 h, the process slows down. Behind this phenomenon, three degradation mechanisms coexist: carbon corrosion, crystallite migration and 3D Ostwald ripening. The surface-averaged mean particle size increases continuously upon ageing (Fig. 3), but this increase remains small (+1.2 nm in 3422 h) due to the moderate chemical potential of Pt$_3$Co/C crystallites *ca.* 4–5 nm in size, with respect to nanocrystallites smaller than 3 nm in diameter [69].

3.1.3. At the nanometre scale: carbon corrosion

The catalyst layers were also examined by LASER Raman spectroscopy to detect possible variations of the structural order of the carbon support. The Raman spectra measured on the fresh/aged
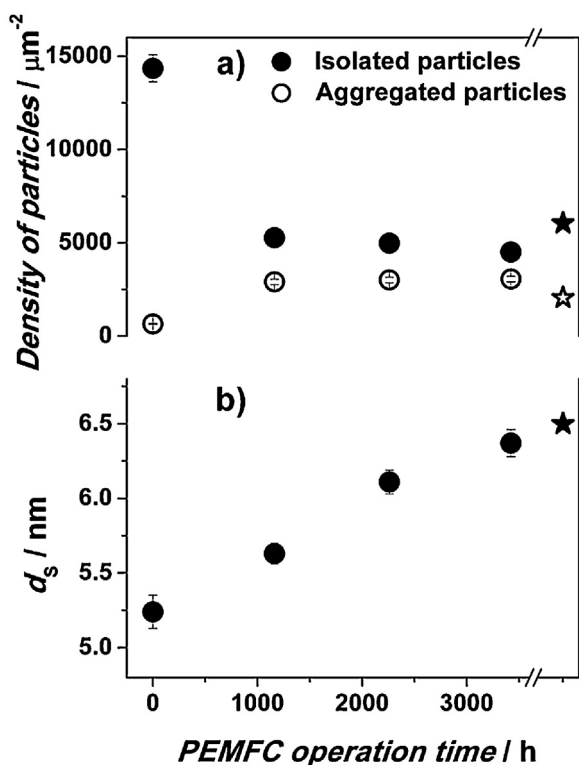
Fig. 3. (a) Density of isolated and aggregated Pt–Co/C nanoparticles per geometric μm² of carbon and (b) surface-averaged diameter ($\overline{d}_S$) statically estimated by measuring the size of isolated Pt–Co/C particles *vs.* PEMFC operation time. The star symbols display the values measured on Pt/C 40 wt.% (E-TeK) used as a reference material.

Fig. 4. (a) Normalized Raman spectra of the fresh/aged Pt–Co/C cathode electrocatalysts before/after operation at $I = 50$ A–$T = 70$ °C–65% RH for various durations, (b) variation of the ratio of the integrated intensities of the D and G bands $I(D)/I(G)$, and of the mean crystallite size of the nanostructured carbon support (L_a).

carbon support (Fig. 4a) present typical characteristics of carbon black materials: the weak band at 1595 cm^{-1} is ascribed to the ordered graphitic structure (*G* band) while disorder-induced *D* and *D′* bands at 1355 and 1615 cm^{-1}, respectively are attributed to defects in the graphite structure [70,71]. These bands are present in the Raman spectra of the fresh carbon support, suggesting that disordered (*D* bands) and graphitized (*G* band) domains coexist. However, the intensity of the *D* band is more severely depreciated than that of the *G* band during PEMFC operation, providing evidence of structure sensitive corrosion kinetics (Fig. 4b). After 2259 h of operation, a narrowing of the high frequency band is observed, most likely because the *D′* band has nearly disappeared (Fig. 4a). Interestingly, after 3422 h of operation, the *G* band also decreases in intensity, indicating that the ordered graphitic domains have suffered degradation at this stage. This hypothesis is further supported by the decrease in intensity of the (0 0 2) reflection of graphite at $2\theta \sim 26.1°$ in X-ray diffraction experiments (Fig. 5a). These experimental results suggest the gradual conversion of ordered graphitic domains into disordered domains, that is amorphization of the structure of the high surface area carbon support, as previously put forth by More et al. [72,73].

Similar to what was observed for the metal nanoparticles; it is striking that the structural changes are fast during the first 1163 h of operation and then slow down. This is reflected by the variation of the carbon mean crystallite size (L_a) *vs.* the PEMFC operation time (L_a being derived from the $I(D)/I(G)$ ratio using the Knight and White formula [74,75]). The L_a value increases upon ageing (until $t = 2259$ h, Fig. 4b), indicating that the aged carbon support is indeed (in average) more graphitic than the fresh one, but the trend is mildly reversing for longer durations, in agreement with the carbon-oxidation (amorphization) scenario proposed above. Another interesting result is the close parallel
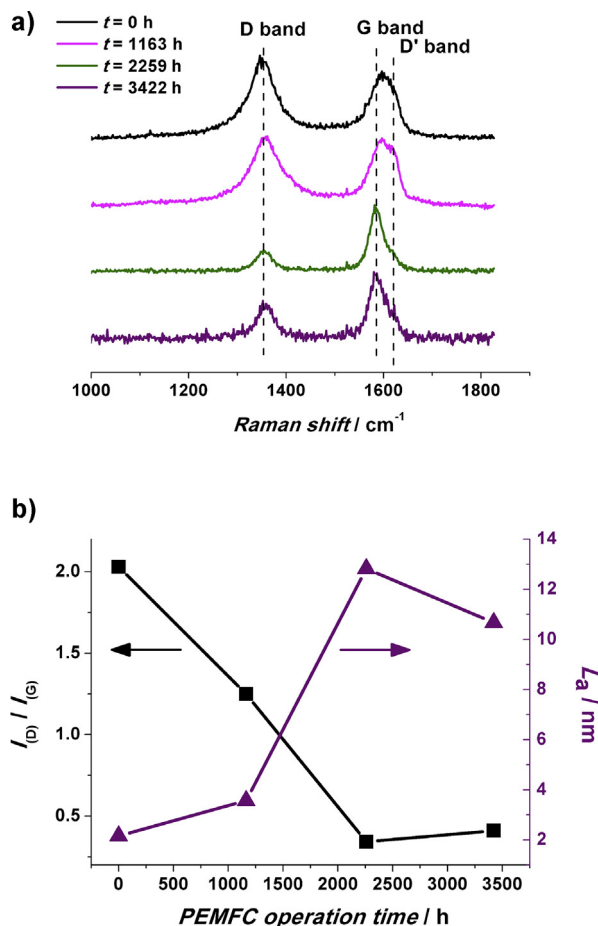
between the variations of the density of aggregated Pt–Co/C particles and the carbon corrosion rate (semi-quantitatively monitored by the evolution of the cathode thickness), which is fast in the first 1163 h of operation and then slower. This result nicely confirms our previous suggestion [76,77] that metal nanoparticles strongly interact with the disordered domains of the carbon support, most likely via the oxygen-containing groups (the fraction of which is proportional to the degree of disorder of the carbon black nanoparticles) [78].

3.2. Compositional and structural changes of the Pt–Co/C nanoparticles

The X-ray diffraction patterns displayed in Fig. 5a indicate that the fresh Pt–Co/C cathode electrocatalyst is of face-centred cubic structure and that Pt and Co atoms are alloyed. However, the progressive shift of the reflections towards smaller 2θ angles upon ageing signs the gradual depletion of the smallest element (Co). Also, whereas the XRD pattern measured on the fresh catalyst features a single peak attributed to an average alloy composition close to Pt$_3$Co, the aged ones typically feature two main contributions, suggesting the coexistence of (at least) 2 metal phases (Fig. 5a, inset).

To gain some insights into the structural and compositional evolution of the fresh Pt$_3$Co/C catalyst, electron energy loss spectra (EELS) in SI mode were recorded on the fresh and the 3422 h aged cathode. As mentioned in Section 2.3, in this
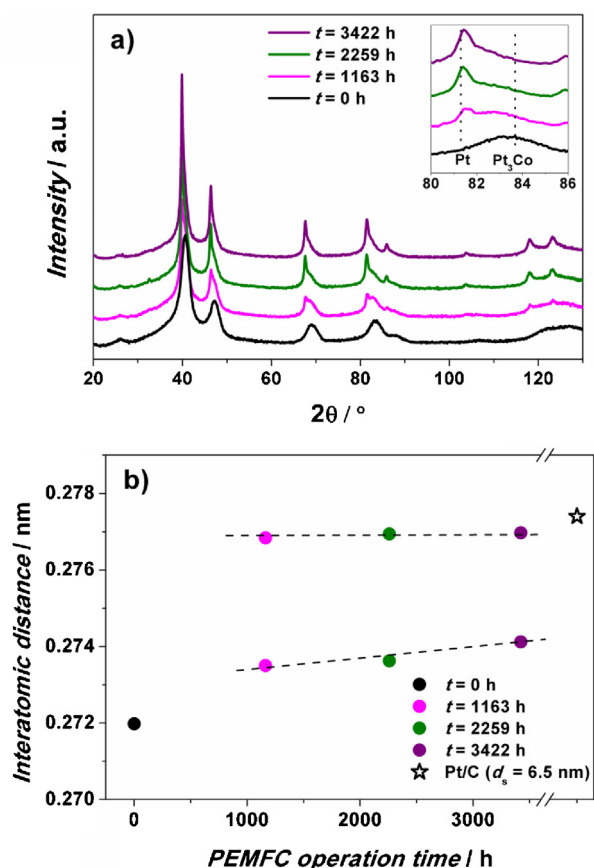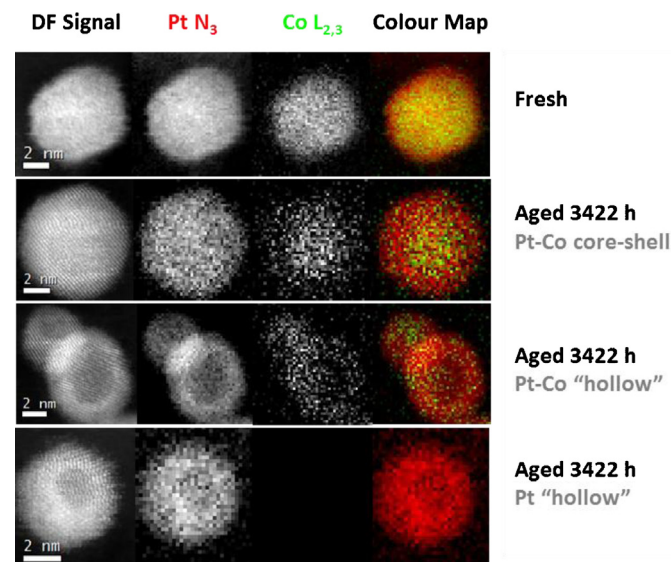
Fig. 5. (a) X-ray diffraction patterns of the Pt–Co/C cathode material upon operation at 50 A/70 °C/65% RH for different durations. Inset: zoom for 2θ comprised between 80 and 86° showing the contribution of the two phases, pure Pt corresponding to the shell of Pt hollow particles and Pt–Co alloyed particles and (b) Evolution of the inter-atomic distance of both phases (Pt and Pt–Co alloy) with the operating time. The two dashed lines present in Fig. 5b serve as a visual guide to estimate the variation of the interatomic distance for both the Co-rich and the Pt-rich metal phases.


Fig. 6. HAADF signal of individual nanoparticles acquired simultaneously with the EELS spectra. The elemental maps were constructed using the Pt N_3 (518 eV) and the Co-$L_{2,3}$ (780 eV) edges, respectively. The Pt N_3 signal is shown in red, and the Co $L_{2,3}$ signal is shown in green. The reader is referred to Supplementary information S1–S4 for the extraction of the Pt N_3 or the Co $L_{2,3}$ edge using a power law background subtraction method.

mode, one EEL spectrum and the high angle annular dark field (HAADF) signal are both collected at each point of the electron beam scan, which allows correlating the nanoanalytical and nanostructural information at the atomic scale. The extraction of the Pt N_3 or the Co $L_{2,3}$ edge using a power law background subtraction method is documented in Supplementary information S1–S4 for the fresh/aged nanoparticles. Three different structures are identified in the aged cathode catalytic layer (Fig. 6):

- "core–shell" nanoparticles composed of a 3–5 atomic layer Pt-rich shell covering a Co-depleted core. Such structures are classically observed after electrochemical dealloying or long-term PEMFC operation of Pt–Co/C materials [8,35,36,79].
- "Hollow" Pt–Co/C nanoparticles (i.e. containing a cavity in their centre) containing limited amount of Co atoms distributed at the atomic scale.
- Pure "hollow" Pt/C nanoparticles containing Co neither in the core, nor in the shell. This type of nanostructure suggests complete dissolution of Co atoms, and is therefore believed to be the ultimate stage from the transformation of the initial Pt$_3$Co alloy via that of "hollow" Pt–Co/C nanoparticles.

In our previous study, [36] the depletion in Co and the formation of Pt "hollow" nanoparticles was accounted for by a nanoscale Kirkendall effect in which the fast diffusion of Co atoms outwards was counterbalanced by a flux of vacancies entering the material,

and yielding formation of closed pores in the centre of the nanoparticles. Based on the fact that such structures were found in PEMFC catalytic layers only when the potential of the cathode exceed that of surface oxide formation ($E \approx 0.60$ V vs. RHE on pure Pt/C), we argued that the formation of surface oxides from water was key to the formation of these nanostructures. The results found in this study confirm this theory since the average cell voltage measured on 6 cells was above 0.55 V for more than 2000 h (see Supplementary information Figure S5). Recently, using STEM-HAADF images, we also suggested [63,80] that the fraction of Pt "hollow" particles could be regarded a fingerprint of the effectiveness factor of the catalytic layers. Indeed, hollow nanoparticles are frequently found in the zones of the CL, where other structural markers (such as the increase of the mean particle size and the densities of isolated/aggregated particles) strongly suggest that they were correctly utilized during the PEMFC operation. At variance, other zones of the catalytic layer featured well-distributed particles on the carbon support, with uniform contrast in STEM-HAADF and Co at.% < 5–10 at.% in local X-EDS analyses: clearly these regions were probably not at the triple phase boundary or insufficiently fed with oxygen during PEMFC operation (low effectiveness factor).

At the light of the STEM-EELS results, the two types of reflections observed on aged Pt–Co/C samples in XRD experiments likely reflect diffraction from the Co-depleted cores or from the Pt-rich shell present in the aged metal nanoparticles. To support this hypothesis, the average inter-atomic distance of the two phases is plotted in Fig. 5b. The average inter-atomic distance of the Pt–Co alloyed phase increases over time confirming the continuous dissolution of Co atoms during the long-term ageing test. Here again, two regimes occur: fast dissolution of the Co-rich phase is observed at the beginning of the ageing test followed by slower dissolution for $t > 1163$ h. At variance, the Pt-rich phase, once it has formed, remains stable for more than 2000 h, as shown by its constant interatomic distance (0.2769 nm). It is striking that this value is nearly identical to that measured on "hollow" nanoparticles obtained from Pt$_3$Co/C electrocatalysts aged in different conditions (0.2766 nm) [34,35]. This result has large implications in terms of durability and catalytic activity of bimetallic Pt–Co/C materials. Firstly, it is undeniable proof that, after complete Co dissolution, the "hollow"
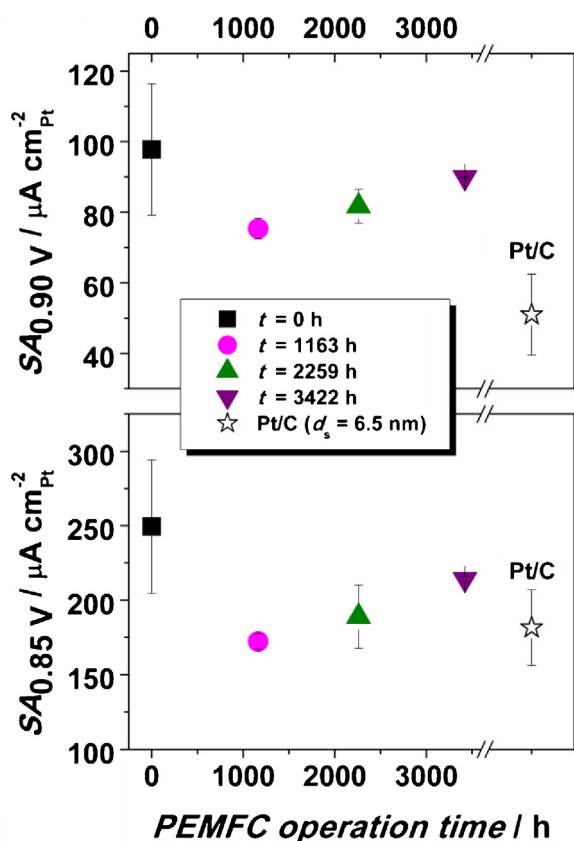
Fig. 7. Specific activity of Pt–Co/C electrodes for the ORR reported at $E = 0.85$ or 0.90 V *vs.* RHE *vs.* the PEMFC operation time. Porous RDE – electrolyte: 0.1 mol dm^{-3} H$_2$SO$_4$ – $T = 298 \pm 1$ K – $v = 2$ mV s^{-1} – positive going potential scan from 0.40 to 1.05 V *vs.* RHE. The specific activities for the ORR have been normalized to the Pt surface area determined by CO stripping coulometry. Each point is the averaged value of at least three measurements; the error bars represent the standard deviation.

nanoparticles are stable in structure and shape. Secondly, the slight contraction of the inter-atomic distance of the Pt-rich shell with respect to the value measured on pure Pt/C nanocrystallites of the same size (star symbol in Fig. 5b) is important because it helps rationalizing the better ORR activity of "hollow" with respect to "bulk" Pt/C nanocrystallites [35,36,81,82]. Indeed, the small compression of the Pt–Pt interatomic distance observed in the Pt-rich phase (outer Pt-rich shell in "hollow" or core/shell nanoparticles) weakens the adsorption energies and the intramolecular bond energies of OH and ORR intermediates relative to pure Pt, thereby positively affecting the rate of the ORR [83,84]. Here again, the relationships between structure, ORR catalytic activity and durability are obvious (Fig. 7). While the intrinsic catalytic activity of the Pt–Co/C materials decreases during the first 1163 h of operation due to the loss of Co atoms (see Fig. 5), the formation of the "hollow" Pt and Pt–Co/C nanoparticles allows restoring, and then maintaining the specific activity at a higher value than "bulk" Pt/C.

It is also interesting to note that the bimetallic catalysts largely improve the ORR catalytic activity with respect to pure Pt/C at $E = 0.90$ V *vs.* RHE, and that the kinetic differences level off at lower electrode potential ($E = 0.85$ V *vs.* RHE). Clearly, the different trends are linked to the increasing coverage of the catalyst surface by oxides with the electrode potential. This goes in line with the results obtained by Wakisaka *et al.* [9] in combined electrochemical-X-ray photoelectron spectroscopy: the better ORR activity of "Pt-skin" catalysts compared to pure Pt was correlated with the higher coverage of O$_{ads}$ species, and with the smaller coverage with H$_2$O$_{ads}$ on the bimetallic surfaces.

4. Conclusions

In this study, the compositional and the structural changes of Pt$_3$Co/C nanocatalysts were surveyed during PEMFC operation for $t = 3422$ h. Two kinetic regimes of ageing were experimentally put forth:

- During the first 1163 h of operation, the composition and structure of the fresh Pt$_3$Co/C nanoparticles suffer drastic changes, signing the occurrence of: (i) Co dissolution, (ii) 3D Ostwald ripening, (iii) crystallite migration, and (iv) corrosion of the high surface area carbon support. A new metal phase is detected by XRD at $t = 1163$ h, which was ascribed from STEM-EELS results to the Pt-rich shell forming in "hollow" and core/shell nanoparticles.
- From 1163 h to 3422 h of operation, the degradation rate of the catalysts slows down without stopping, and the number of observed "hollow" and core/shell Pt-rich nanoparticles increases, their structure remaining largely unchanged. The absence of relaxation of the lattice parameter of the Pt-rich shell over more than 2000 h of operation signs its long-term stability. It is believed that the "final" structure of Pt$_3$Co/C nanoparticles after PEMFC operation is Pt "hollow"/C nanoparticles from which all Co has been depleted. The corrosion of the high surface area carbon support also proceeds during this time period, but with slower kinetics due to the higher corrosion-resistance of the graphitized domains of the carbon black support (the carbon support is more graphitic in average once the disordered domains have preferentially been corroded into CO$_2$).

The results presented in this study illustrate that some regions of the cathode catalytic layer are more easily corroded than others in PEMFC operating conditions. At both the micrometre and nanometre scales, the degradation mechanisms proceed fastly at structural defects, which are: (i) the disordered crystallographic domains of the carbon support (carbon corrosion), (ii) the smallest metal nanocrystallites (electrochemical-Ostwald ripening), and (iii) the Co atoms present in the near-surface layers of the bimetallic Pt-based Pt–Co/C nanoparticles (Co dissolution). The major discovery of this study is the ability of the Pt-rich phase formed on aged Pt–Co/C nanoparticles to withstand continuous PEMFC operation for more than 2000 h without structural degradation. The robustness of the Pt-rich phase translates into a stabilization, and even a slight increase of the ORR intrinsic catalytic activity. This is an important aspect for the development of robust and highly active ORR electrocatalysts.

Acknowledgements

Appendix A. Supplementary data

Supplementary data associated with this article can be found, in the online version, at http://dx.doi.org/10.1016/j.apcatb.2013.06.011.

References

[1] F.T. Wagner, B. Lakshmanan, M.F. Mathias, Journal of Physical Chemistry Letters 1 (2010) 2204–2219.
[2] M. Watanabe, K. Tsurumi, T. Mizukami, T. Nakamura, P. Stonehart, Journal of the Electrochemical Society 141 (1994) 2659–2668.

[3] T. Toda, H. Igarashi, H. Uchida, M. Watanabe, Journal of the Electrochemical Society 146 (1999) 3750–3756.

[4] E. Antolini, J.R.C. Salgado, E.R. Gonzalez, Journal of Electroanalytical Chemistry 580 (2005) 145–154.

[5] E. Antolini, J.R.C. Salgado, E.R. Gonzalez, Journal of Power Sources 160 (2006) 957–968.

[6] V.R. Stamenkovic, B.S. Mun, M. Arenz, K.J.J. Mayrhofer, C.A. Lucas, G.F. Wang, P.N. Ross, N.M. Markovic, Nature Materials 6 (2007) 241–247.

[7] H. Yano, M. Kataoka, H. Yamashita, H. Uchida, M. Watanabe, Langmuir 23 (2007) 6438–6445.

[8] S.C. Zignani, E. Antolini, E.R. Gonzalez, Journal of Power Sources 182 (2008) 83–90.

[9] M. Wakisaka, H. Suzuki, S. Mitsui, H. Uchida, M. Watanabe, Journal of Physical Chemistry C 112 (2008) 2750–2755.

[10] R.Z. Yang, J. Leisch, P. Strasser, M.F. Toney, Chemistry of Materials 22 (2010) 4712–4720.

[11] T. Toda, H. Igarashi, M. Watanabe, Journal of the Electrochemical Society 145 (1998) 4185–4188.

[12] M.K. Min, J.H. Cho, K.W. Cho, H. Kim, Electrochimica Acta 45 (2000) 4211–4217.

[13] V.R. Stamenkovic, B. Fowler, B.S. Mun, G.F. Wang, P.N. Ross, C.A. Lucas, N.M. Markovic, Science 315 (2007) 493–497.

[14] C.H. Cui, L. Gan, H.H. Li, S.H. Yu, M. Heggen, P. Strasser, Nano Letters 12 (2012) 5885–5889.

[15] V.R. Stamenkovic, B.S. Mun, K.J.J. Mayrhofer, P.N. Ross, N.M. Markovic, Journal of the American Chemical Society 128 (2006) 8813–8819.

[16] S. Chen, W. Sheng, N. Yabuuchi, P.J. Ferreira, L.F. Allard, Y. Shao-Horn, Journal of Physical Chemistry C 113 (2009) 1109–1125.

[17] D. Wang, Y. Yu, H.L. Xin, R. Hovden, P. Ercius, J.A. Mundy, H. Chen, J.H. Richard, D.A. Muller, F.J. Disalvo, H.D. Abruña, Nano Letters 12 (2012) 5230–5238.

[18] D. Wang, H.L. Xin, R. Hovden, H. Wang, Y. Yu, D.A. Muller, F.J. Disalvo, H.D. Abruña, Nature Materials 12 (2013) 81–87.

[19] S. Koh, P. Strasser, Journal of the American Chemical Society 129 (2007) 12624–12625.

[20] J.C. Canullo, W.E. Triaca, A.J. Arvia, Journal of Electroanalytical Chemistry and Interfacial Electrochemistry 200 (1986) 397–400.

[21] K. Matsuzawa, T. Fukushima, M. Inaba, Electrocatalysis 1 (2010) 169–177.

[22] P. Urchaga, S. Baranton, T. Napporn, C. Coutanceau, Electrocatalysis 1 (2010) 3–6.

[23] C. Coutanceau, P. Urchaga, S. Brimaud, S. Baranton, Electrocatalysis 3 (2012) 75–87.

[24] K. Sasaki, Y. Mo, J.X. Wang, M. Balasubramanian, F. Uribe, J. McBreen, R.R. Adzic, Electrochimica Acta 48 (2003) 3841–3849.

[25] J. Zhang, F.H.B. Lima, M.H. Shao, K. Sasaki, J.X. Wang, J. Hanson, R.R. Adzic, Journal of Physical Chemistry B 109 (2005) 22701–22704.

[26] F. Jaouen, S. Marcotte, J.P. Dodelet, G. Lindbergh, Journal of Physical Chemistry B 107 (2003) 1376–1386.

[27] F. Jaouen, E. Proietti, M. Lefevre, R. Chenitz, J.P. Dodelet, G. Wu, H.T. Chung, C.M. Johnston, P. Zelenay, Energy & Environmental Science 4 (2011) 114–130.

[28] J. Suntivich, H.A. Gasteiger, N. Yabuuchi, H. Nakanishi, J.B. Goodenough, Y. Shao-Horn, Nature Chemistry 3 (2011) 546–550.

[29] G. Wu, K.L. More, C.M. Johnston, P. Zelenay, Science 332 (2011) 443–447.

[30] C. Wang, M. Chi, D. Li, D. Strmcnik, D. Van Der Vliet, G. Wang, V. Komanicky, K.C. Chang, A.P. Paulikas, D. Tripkovic, J. Pearson, K.L. More, N.M. Markovic, V.R. Stamenkovic, Journal of the American Chemical Society 133 (2011) 14396–14403.

[31] S.C. Ball, S.L. Hudson, J.H. Leung, A.E. Russell, D. Thompsett, B.R. Theobald, ECS Transactions 11 (2007) 1247–1257.

[32] F. Maillard, L. Dubau, J. Durst, M. Chatenet, J. André, E. Rossinot, Electrochemistry Communications 12 (2010) 1161–1164.

[33] S. Chen, H.A. Gasteiger, K. Hayakawa, T. Tada, Y. Shao-Horn, Journal of the Electrochemical Society 157 (2010) A82–A97.

[34] L. Dubau, F. Maillard, M. Chatenet, L. Guétaz, J. Andre, E. Rossinot, Journal of the Electrochemical Society 157 (2010) B1887–B1895.

[35] L. Dubau, F. Maillard, M. Chatenet, J. André, E. Rossinot, Electrochimica Acta 56 (2010) 776–783.

[36] L. Dubau, J. Durst, F. Maillard, L. Guétaz, M. Chatenet, J. André, E. Rossinot, Electrochimica Acta 56 (2011) 10658–10667.

[37] Y. Ma, P.B. Balbuena, Surface Science 602 (2008) 107–113.

[38] R. Callejas-Tovar, W.T. Liao, H. Mera, P.B. Balbuena, Journal of Physical Chemistry C 115 (2011) 23768–23777.

[39] P.B. Balbuena, R. Callejas-Tovar, P. Hirunsit, J.M. Martínez De La Hoz, Y. Ma, G.E. Ramírez-Caballero, Topics in Catalysis 55 (2012) 322–325.

[40] R. Callejas-Tovar, P.B. Balbuena, Journal of Physical Chemistry C 116 (2012) 14414–14422.

[41] J. Durst, M. Chatenet, F. Maillard, Physical Chemistry Chemical Physics 14 (2012) 13000–13009.

[42] J. Erlebacher, M.J. Aziz, A. Karma, N. Dimitrov, K. Sieradzki, Nature 410 (2001) 450–453.

[43] M. Oezaslan, M. Heggen, P. Strasser, Journal of the American Chemical Society 134 (2012) 514–524.

[44] L. Gan, M. Heggen, R. O'Malley, B. Theobald, P. Strasser, Nano Letters 13 (2013) 1131–1138.

[45] J. Erlebacher, Journal of the Electrochemical Society 151 (2004) C614–C626.

[46] I. Dutta, M.K. Carpenter, M.P. Balogh, J.M. Ziegelbauer, T.E. Moylan, M.H. Atwan, N.P. Irish, Journal of Physical Chemistry C 114 (2010) 16309–16320.

[47] Y. Yu, H.L. Xin, R. Hovden, D. Wang, E.D. Rus, J.A. Mundy, D.A. Muller, H.D. Abruna, Nano Letters 12 (2012) 4417–4423.

[48] D.A. Stevens, S. Wang, R.J. Sanderson, G.C.K. Liu, G.D. Vernstrom, R.T. Atanasoski, M.K. Debe, J.R. Dahn, Journal of the Electrochemical Society 158 (2011) B899–B904.

[49] J. Snyder, I. McCue, K. Livi, J. Erlebacher, Journal of the American Chemical Society 134 (2012) 8633–8645.

[50] J.E. Harlow, D.A. Stevens, R.J. Sanderson, G.C.K. Liu, L.B. Lohstreter, G.D. Vernstrom, R.T. Atanasoski, M.K. Debe, J.R. Dahn, Journal of the Electrochemical Society 159 (2012) B670–B676.

[51] F. Maillard, A. Bonnefont, F. Micoud, Electrochemistry Communications 13 (2011) 1109–1111.

[52] J. Willsau, J. Heitbaum, Journal of Electroanalytical Chemistry 161 (1984) 93–101.

[53] L.M. Roen, C.H. Paik, T.D. Jarvi, Electrochemical and Solid-State Letters 7 (2004) A19–A22.

[54] D.A. Stevens, J.R. Dahn, Carbon 43 (2005) 179–188.

[55] S. Maass, F. Finsterwalder, G. Frank, R. Hartmann, C. Merten, Journal of Power Sources 176 (2008) 444–451.

[56] F. Coloma, A. Sepulveda-Escribano, F. Rodriguez-Reinoso, Journal of Catalysis 154 (1995) 299–305.

[57] K. Kinoshita, Carbon, Electrochemical and Physicochemical Properties, John Wiley & Sons, New York, 1988.

[58] M. Hara, M. Lee, C.-H. Liu, B.-H. Chen, Y. Yamashita, M. Uchida, H. Uchida, M. Watanabe, Electrochimica Acta 70 (2012) 171–181.

[59] C.A. Reiser, L. Bregoli, T.W. Patterson, J.S. Yi, J.D.L. Yang, M.L. Perry, T.D. Jarvi, Electrochemical and Solid State Letters 8 (2005) A273–A276.

[60] G. Maranzana, C. Moyne, J. Dillet, S. Didierjean, O. Lottin, Journal of Power Sources 195 (2010) 5990–5995.

[61] J. Durst, A. Lamibrac, F. Charlot, J. Dillet, L.F. Castanheira, G. Maranzana, L. Dubau, F. Maillard, M. Chatenet, O. Lottin, Applied Catalysis B: Environmental 138–139 (2013) 416–426.

[62] A. Lamibrac, G. Maranzana, O. Lottin, J. Dillet, J. Mainka, S. Didierjean, A. Thomas, C. Moyne, Journal of Power Sources 196 (2011) 9451–9458.

[63] L. Dubau, J. Durst, F. Maillard, M. Chatenet, J. André, E. Rossinot, Fuel Cells 12 (2012) 188–198.

[64] F. de la Peña, M.H. Berger, J.F. Hochepied, F. Dynys, O. Stephan, M. Walls, Ultramicroscopy 111 (2011) 169–176.

[65] H.L. Xin, J.A. Mundy, Z. Liu, R. Cabezas, R. Hovden, L.F. Kourkoutis, J. Zhang, N.P. Subramanian, R. Makharia, F.T. Wagner, D.A. Muller, Nano Letters 12 (2012) 490–497.

[66] P.J. Ferreira, G.J. la O', Y. Shao-Horn, D. Morgan, R. Makharia, S. Kocha, H.A. Gasteiger, Journal of the Electrochemical Society 152 (2005) A2256–A2271.

[67] E. Guilminot, A. Corcella, F. Charlot, F. Maillard, M. Chatenet, Journal of the Electrochemical Society 154 (2007) B96–B105.

[68] P.J. Ferreira, Y. Shao-Horn, Electrochemical and Solid State Letters 10 (2007) B60–B63.

[69] Y. Shao-Horn, W. Sheng, S. Chen, P. Ferreira, E. Holby, D. Morgan, Topics in Catalysis 46 (2007) 285–305.

[70] F. Tuinstra, J.L. Koenig, Journal of Chemical Physics 53 (1970) 1126–1130.

[71] L.G. Cancado, K. Takai, T. Enoki, M. Endo, Y.A. Kim, H. Mizusaki, A. Jorio, L.N. Coelho, R. Magalhaes-Paniago, M.A. Pimenta, Applied Physics Letters 88 (2006) 163103–163106.

[72] Z.Y. Liu, J.L. Zhang, P.T. Yu, J.X. Zhang, R. Makharia, K.L. More, E.A. Stach, Journal of the Electrochemical Society 157 (2010) B906–B913.

[73] K.L. More, R. Perry, M. Chi, S. Reeves, ECS Meeting Abstracts, Las Vegas, NV, USA, 2010, p. 611.

[74] T. Jawhari, A. Roid, J. Casado, Carbon 33 (1995) 1561–1565.

[75] D.S. Knight, W.B. White, Journal of Materials Research 4 (1989) 385–393.

[76] Z. Zhao, L. Castanheira, L. Dubau, G. Berthomé, A. Crisci, F. Maillard, Journal of Power Sources 230 (2013) 236–243.

[77] L. Dubau, L. Castanheira, G. Berthomé, F. Maillard, Electrochimica Acta (2013), http://dx.doi.org/10.1016/j.electacta.2013.03.184.

[78] Z. Zhao, L. Dubau, F. Maillard, Journal of Power Sources 217 (2012) 449–458.

[79] P. Yu, M. Pemberton, P. Plasse, Journal of Power Sources 144 (2005) 11–20.

[80] L. Dubau, L. Guétaz, J. Durst, F. Maillard, M. Chatenet, J. André, E. Rossinot, ECS Electrochemistry Letters 1 (2012) F13–F15.

[81] D.A. Cantane, F.E.R. Oliveira, S.F. Santos, F.H.B. Lima, Applied Catalysis B: Environmental 136–137 (2013) 351–360.

[82] J.X. Wang, C. Ma, Y.M. Choi, D. Su, Y.M. Zhu, P. Liu, R. Si, M.B. Vukmirovic, Y. Zhang, R.R. Adzic, Journal of the American Chemical Society 133 (2011) 13551–13557.

[83] T. Bligaard, J.K. Nørskov, Electrochimica Acta 52 (2007) 5512–5516.

[84] Y. Xu, A.V. Ruban, M. Mavrikakis, Journal of the American Chemical Society 126 (2004) 4717–4725.